REPORT DOCUMENTATION PAGE

Form Approved
OMB No. 0704-0188

1. REPORT DATE *(DD-MM-YYYY)*	**2. REPORT TYPE**	**3. DATES COVERED** *(From - To)*
12/4/2023	Technical Report	Oct, 2021 - Nov, 2023

4. TITLE AND SUBTITLE

Investigation of La0.7Sr0.3VO3.86-δ (LSV) Vanadium Oxidation Number and Oxygen Stoichiometry from Experimental Optical Microscopy Characterization and Rietveld Refinement Calculations

5a. CONTRACT NUMBER

5b. GRANT NUMBER

5c. PROGRAM ELEMENT NUMBER
6.1 Funding

6. AUTHOR(S)
Talia M. Sebastian
Theodore E. Burye

5d. PROJECT NUMBER

5e. TASK NUMBER

5f. WORK UNIT NUMBER

7. PERFORMING ORGANIZATION NAME(S) AND ADDRESS(ES)
US Army Development Command (DEVCOM)
Ground Vehicle Systems Center (GVSC)
Ground Vehicle Power and Mobility (GVPM)
Force Projection Technology (FPT)
6501 E. 11 Mile Road
Warren, MI 48397

8. PERFORMING ORGANIZATION REPORT NUMBER
OPSEC 8156

9. SPONSORING / MONITORING AGENCY NAME(S) AND ADDRESS(ES)
US Army Development Command (DEVCOM)
Ground Vehicle Systems Center (GVSC)
Ground Vehicle Power and Mobility (GVPM)
Force Projection Technology (FPT)
6501 E. 11 Mile Road

10. SPONSOR/MONITOR'S ACRONYM(S)

11. SPONSOR/MONITOR'S REPORT NUMBER(S)

12. DISTRIBUTION / AVAILABILITY STATEMENT
DISTRIBUTION STATEMENT A. Approved for public release; distribution is unlimited. OPSEC #8156

13. SUPPLEMENTARY NOTES

14. ABSTRACT

15. SUBJECT TERMS

16. SECURITY CLASSIFICATION OF: Available for Public Release			**17. LIMITATION OF ABSTRACT**	**18. NUMBER OF PAGES**	**19a. NAME OF RESPONSIBLE PERSON**
a. REPORT	**b. ABSTRACT**	**c. THIS PAGE**	Same as Report (SAR)	34	Theodore Burye
UNCLS	UNCLAS	UNCLAS			**19b. TELEPHONE NUMBER** *(include area code)* 586-282-3047

Investigation of $La_{0.7}Sr_{0.3}VO_{3.86-\delta}$ (LSV) Vanadium Oxidation Number and Oxygen Stoichiometry from Experimental Optical Microscopy Characterization and Rietveld Refinement Calculations

Talia Sebastian[a] & Theodore Burye[b]
U.S. Army Development Command (DEVCOM) Ground Vehicle Systems Center (GVSC)
Force Projection Technology[a], Ground Vehicle Power & Mobility[b]

Prepared by:

Dr. Talia Sebastian
Research Chemist
talia.m.sebastian.civ@army.mil
Fuels and Lubricants Branch
Force Protection Technology (FPT)
U.S. Army Development Command (DEVCOM) Ground Vehicle Systems Center (GVSC)

Dr. Theodore Burye
Chemical Engineer
theodore.e.burye2.civ@army.mil
Fuel Cell Technologies
Ground Vehicle Power and Mobility (GVPM)
U.S. Army Development Command (DEVCOM) Ground Vehicle Systems Center (GVSC)

Acknowledgements

X-ray Diffraction (XRD) data were acquired from the Ground Vehicle Systems Centers (GVSC's) Metallurgy Laboratory. Demetrios Tzelepis and Ian Toppler, from the Characterization & Failure Analysis Group, assisted with operation of the XRD equipment.

Scanning Electron Microscopy (SEM) and Energy Dispersive Spectroscopy (EDS) data were acquired from the Ground Vehicle Systems Centers (GVSC's) Metallurgy Laboratory. Demetrios Tzelepis and Ian Toppler, from the Characterization & Failure Analysis group, assisted with operation of the SEM/EDS equipment.

Optical Microscopy images were acquired from the GVSC's Fuel Cell Technologies Laboratory.

Table of Contents

List of Figures

List of Tables

1.0 Introduction

The purpose of this effort was to analyze optical color differences in the $La_{0.7}Sr_{0.3}VO_{3.86-\delta}$ (LSV) material (i.e., powder) after being exposed to various 300ppm sulfur-contaminated fuels (i.e., hydrogen (H_2) gas, methane (CH_4) gas, and liquid methanol (CH_3OH)) at operating temperatures between 400-700°C. When the exposed samples were compared their optical properties were observed to be similar after being heated at the same operating temperatures in both hydrogen and methane gas mixtures. Differences in optical properties were observed to emerge with the use of liquid methanol, wherein exposed samples exhibited different sample colors at lower operating temperatures than hydrogen and methane gas exposed samples. Color changes in oxides can be attributed to changes in the oxidation number of transition metal elements, which is vanadium in the case of LSV.

The oxidation number of the vanadium in each exposed sample was determined using Rietveld refinement calculations via X-ray Diffraction (XRD). Adjustments to the Rietveld refinement calculations were made using sulfur concentration measurements collected via SEM/EDS. Understanding changes in the oxidation number of LSV can elucidate internal mechanistic changes and also improve future modeling activities.

2.0 Experimental Methods

2.1 Hydrogen and Methane Gas LSV Experimental Setup, Testing Parameters

Between 2-2.5g of loose neat LSV powder (Praxair Surface Technologies; Woodinville, WA, USA) was placed inside a 99.5% high-purity alumina crucible (LSP Industrial Ceramics, Myrtle Beach, SC, USA) inside a sealed metal sample chamber (i.e., reactor), which was also insulated using high-temperature cloth insulation. This reactor was used to heat the LSV powder in either hydrogen or methane gas contaminated with 300ppm H_2S gas, as shown in **Figure 1**. The use of H_2S, and the concentration used, simulates sulfur exposure from the fuel fed to fuel cell anodes directly or from reformer reformate. Due to the corrosiveness of H_2S gas, especially at elevated temperatures, the sample chamber was constructed from Inconel C-276, which has a high corrosion resistance. All other components, including an inlet extension tube place down inside the alumina crucible to direct gas flow, were constructed using 316 stainless steel (SS). The sample chamber was initially heated using heat tape with a maximum operating temperature of 760°C (Model BW0101020L) from BriskHeat (BriskHeat, Columbus, OH, USA), as shown in **Figure 2**. Later, the heating method was switched to a Leister Hotwind Premium hot air blower (Heely-Brown Company, Atlanta, GA, USA) with a maximum operating temperature of 800°C, as shown in **Figure 3**. An attachment was added to the air blower nozzle to direct the hot air around the sample chamber. The reactor was also reduced in size to fit inside the hot air blower attachment. Nitrogen gas, at 45 PSIG and a 300mL/min flow rate, was directed into the reactor during the heating and cooling process; to prevent LSV samples from oxidizing.

Once the reactor reached its steady-state temperature in each test exposure, 300ppm H_2S with balance hydrogen or methane gas, was introduced into the chamber, simulating anode exposure to hydrogen or light hydrocarbon fuels. Hydrogen sulfide's noncatalytic thermal decomposition temperature has been reported at 1200°C [1], which provides the assumption that hydrogen sulfide

should be stable until it encounters LSV material. Methane has a similar noncatalytic thermal decomposition temperature of 1200°C [2, 3] and therefore is assumed to also remain stable until it encounters LSV material. Both sulfur-containing fuels were fed to the exposed sample in the reactor as 45 PSIG pressure and 300mL/min flow rate, the same as nitrogen gas, which was used initially to purge the reactor prior to exposure. Samples were exposed to the gas while simultaneously being heated between 400-700°C for up to 100 hours. The sample chamber was returned to room temperature every 25 hours for sub-sampling of loose LSV powder, which was subsequently characterized for sulfur content, crystal structure and optical properties.

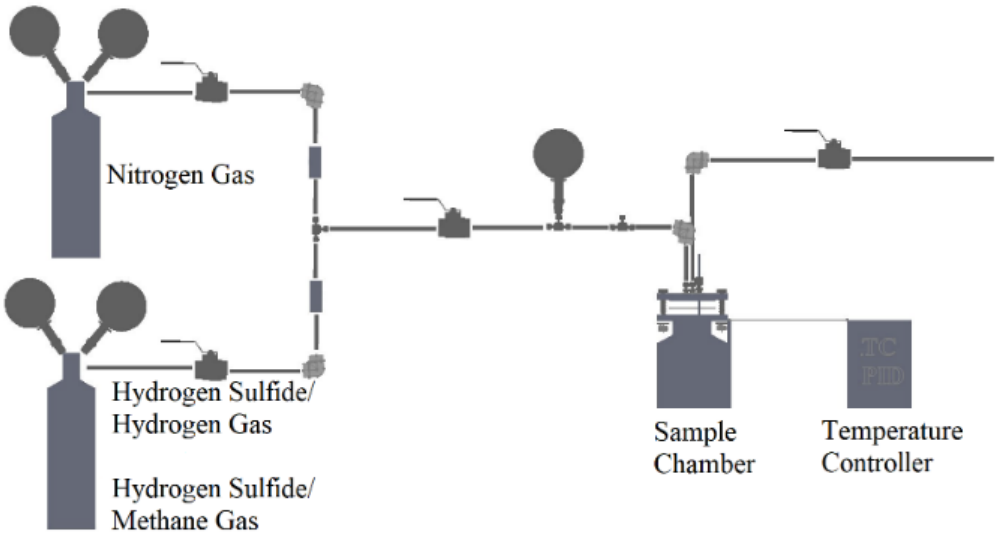

Figure 1: Experimental Setup used for Hydrogen and Methane Fuel Contaminated with 300ppm H_2S.

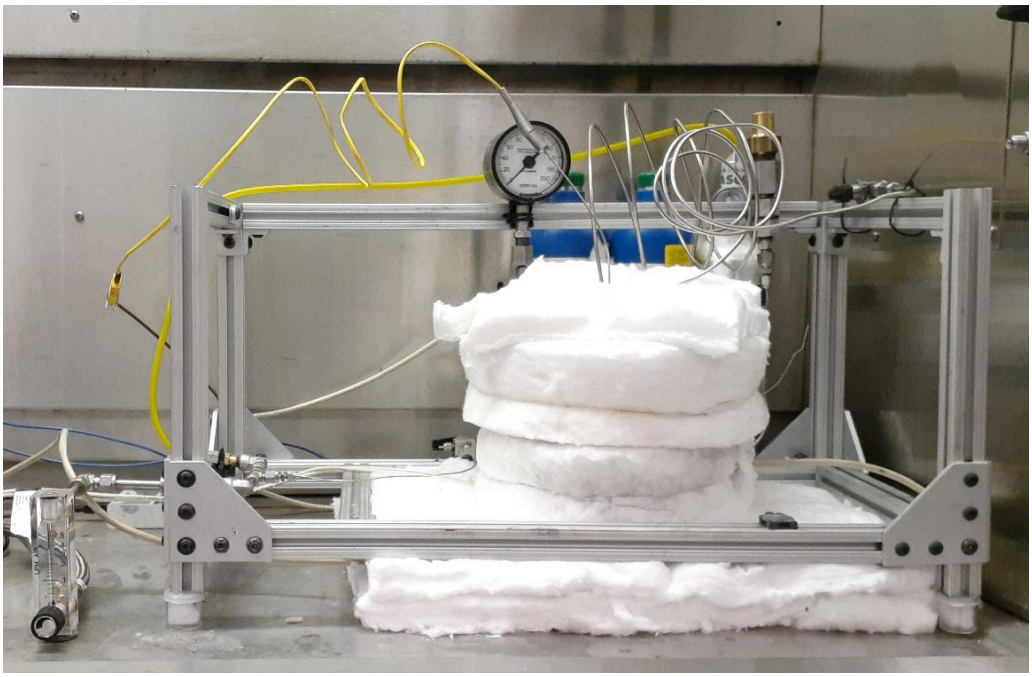

Figure 2: Experimental Reactor Equipment Heated using Heat Tape

Figure 3: Experimental Reactor Equipment Heated using Hot Air Blower

2.2 Methanol Solution LSV Experimental Setup, Testing Parameters

The LSV sample preparation procedures used with the H_2 and CH_4 fuels were also used with the methanol, except for three differences, as shown in **Figure 4**. First, the methanol fuel, which is a liquid at room temperature, was drip-fed into the heated reactor, where it would then vaporize into a gas and interact with the LSV. To achieve this, a peristaltic pump and Tygon™ tubing was used. The flow rate of the liquid methanol was maintained close to 0.13 mL/min. After accounting for volume expansion due to the methanol conversion to a gas, the gaseous methanol flow rate was similar to the 300mL/min flow rate implemented with the hydrogen and methane gas fuels. Second, in the methanol fuel tests, nitrogen was continuously used during heating, cooling and steady-state operation to prevent sample oxidation and to act as an inert carrier gas for methanol vapors. Finally, since methanol fuel is a liquid at room temperature, a liquid sulfur substitute thiophene (C_4H_4S) from Fisher Scientific (ThermoFisher Scientific, Waltham, MA, USA) was used in place of H_2S, since H_2S gas would not maintain a constant concentration in liquid methanol over time. Thiophene is a liquid at room temperature, with a boiling point of 84°C. Thiophene's noncatalytic thermal decomposition temperature has been reported to start at 1226°C [4] , which indicates thiophene will remain stable until exposure to LSV. Methanol's noncatalytic thermal decomposition temperature, on average, is 700°C [5], which may be a factor to consider later in this paper. Thiophene was continuously stirred with methanol, in a glass beaker, to maintain a homogeneous concentration while being pumped into the reactor. The same heating and sample sulfur characterization extraction procedures were used with the methanol fuel exposures, as was previously with the samples using H_2 and CH_4 fuel.

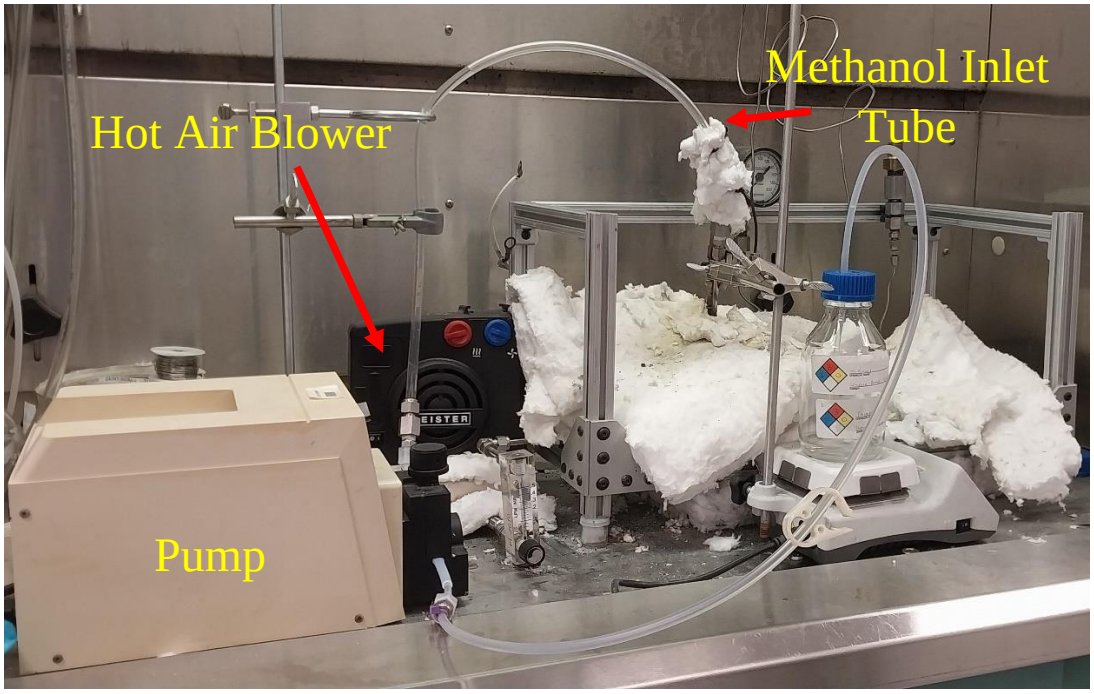

Figure 4: Experimental Setup for Methanol Fuel Contaminated with 300ppm Thiophene

2.3 Characterization Methods

2.3.1 Scanning Electron Microscopy (SEM) and Energy Dispersive Spectroscopy (EDS)

Sulfur peak intensities were measured for each sub-sample using a Hitachi SEM (Hitachi; Krefeld, Germany) with an Oxford Instruments EDS detector (Oxford Instruments; Concord, MA, USA). EDS measurements were taken using a beam voltage of 30.0 kV, a 30 µm aperture, a 512 s scan speed, a 10 mm working distance, and 100x magnification. At least four measurements were taken for each sub-sample and averaged to account for variations.

2.3.2 X-Ray Diffraction (XRD)

XRD was used to characterize changes in each sub-sample crystal structure using a SmartLab XRD (Rigaku Americas Corporation; The Woodlands, TX, USA) operated at 40 kV and 44 mA at room temperature. Scans were taken between $10° \leq 2\theta \leq 90°$ Two-Theta using a 0.020 step, 2.00s scan speed, copper filament and nickel filter. The diffraction peaks were identified from the Inorganic Crystal Structure Database (ICSD).

2.3.3 Optical Microscopy Images

Optical microscopy was used to characterize the color changes of each sub-sample, using a Meiji Techno (Saitama, Japan) EMZ-13TR Trinocular Head with a 1.0x to 7.0x magnification range, combined with a Techniquip (Pleasanton, CA, USA) FOI-150 150W incandescent bulb fiber optic illuminator. A Nikon (Tokyo, Japan) D5600 DSLR camera was attached to the trinocular head to take each image. Each image was taken using a magnification range between 500x-600x an ISO of 100 and shutter speed between 1.0-1.3s in manual mode.

2.4 Experimental Results Calculations

2.4.1 Surface Area Normalized Sulfur Content and Sulfur Accumulation Rate Calculations

Sulfur content in each sub-sample was normalized using the calculated surface area (SA) of aggregate LSV particles from SEM images for each sub-sample operating temperature. Sulfur weight % values (W) were obtained from multiple locations on each sub-sample from SEM/EDS scans and averaged. The average mass of the sulfur was calculated by multiplying the sulfur weight % by the theoretical maximum density (ρ_{msx}) to obtain the average mass of sulfur (M_{sulf}) in each sub-sample. Finally, the sulfur mass in each sub-sample was divided by the average aggregate particle surface area calculated from SEM images to obtain the sulfur mass normalized around sample surface area ($M_{sul,\ norm}$), as shown in **Equations 1-2** below:

$$M_{sulf} = \left(\frac{W}{100}\right) * \rho_{max} \quad \textbf{[1]}$$

$$M_{sulf,norm} = \frac{M_{sulf}}{SA} \quad \textbf{[2]}$$

The sulfur accumulation rate ($R_{sulf,\ acc}$) was calculated by dividing the normalized sulfur mass by the total heating duration (T_{heat}) for each sub-sample, as shown in **Equation 3**:

$$R_{sulf,acc} = \frac{M_{sulf,norm}}{T_{heat}} \quad \textbf{[3]}$$

2.4.2 Rietveld Refinement Oxygen Stoichiometry Calculations

Oxygen stoichiometry in each sub-sample was determined using Rietveld refinement applied to raw XRD spectra. All refinement patterns were visually similar to their respective experimental XRD patterns. XRD diffraction peaks were matched to $LaVO_4$ (Monoclinic, ICSD #8294), $LaVO_4$ (Tetragonal, ICSD #411083), $LaVO_3$ (Cubic, ICSD #28925) and/or $SrVO_3$ (Cubic, ICSD #96291). After the peaks were identified, the phase percentage in each sample was determined along with the oxygen site fractions for each phase. Using the phases identified in each sub-sample, the phase percentage, and the oxygen site fraction an overall oxygen stoichiometry was determined.

2.4.3 Vanadium Oxidation Number Calculations

The oxidation number of vanadium in each sub-sample was determined by accounting for LSVs three cations, lanthanum, strontium and vanadium, and one anion, oxygen. Lanthanum's oxidation number is assumed to be +3, strontium's is +2, and oxygen's is -2. The stoichiometry for lanthanum, strontium and vanadium were already known to be 0.7, 0.3 and 1, respectively, from its formula. The oxygen stoichiometry was determined using the Rietveld refinement process, described above.

By assuming charge neutrality, **Equation 4** was used to back-calculate vanadium's average oxidation number using the assumed lanthanum, strontium and oxygen oxidation states and their stoichiometries.

$$La_{0.7}^{+3} + Sr_{0.3}^{+2} + V_1^x = O_y^{-2} \quad \textbf{[4]}$$

where:

x = vanadium oxidation number

y = Rietveld determined oxygen stoichiometry

The oxidation numbers and stoichiometries for each element was then inserted into **Equation 4** and the equation was solved for the vanadium oxidation number, as shown in **Equation** 5 and **Equation 6**:

$$\big((y)*(-2)\big)-\big((0.7)*(+3)+(0.3)*(+2)\big)=\big((x)*(1)\big) \quad \textbf{[5]}$$

$$\frac{\big((y)*(-2)\big)-\big((0.7)*(+3)+(0.3)*(+2)\big)}{1}=x \quad \textbf{[6]}$$

Equations 4-6 assume an ideal case (i.e. no additional elements considered and an even distribution of lanthanum, strontium and vanadium atoms) for LSV; however, sulfur diffusion into the LSV lattice structure, should also be considered, with respect to phase assignment. Assuming sulfur has an oxidation number of -2, relative stoichiometric amounts were assumed based on the calculated adsorption rates determined using **Equation 3**. As a result, **Equations 4-6** were modified to account for sulfur diffusion into the material, as shown in **Equations 7-9**.

$$La_{0.7}^{+3}+Sr_{0.3}^{+2}+V_1^{x}=O_y^{-2}+S_z^{-2} \quad \textbf{[7]}$$

where:

x = vanadium oxidation number

y= Rietveld determined oxygen stoichiometry

z = sulfur stoichiometry

$$\big((y)*(-2)+(z)*(-2)\big)-\big((0.7)*(+3)+(0.3)*(+2)\big)=\big((x)*(1)\big) \quad \textbf{[8]}$$

$$\frac{\big((y)*(-2)+(z)*(-2)\big)-\big((0.7)*(+3)+(0.3)*(+2)\big)}{1}=x \quad \textbf{[9]}$$

2.4.4 Oxygen Loss Calculations

Oxygen stoichiometry calculations using the Rietveld refinement process did not consider potential changes in oxygen stoichiometry due to the diffusion of sulfur or secondary phase formation. Literature [6, 7, 8, 9, 10, 11] has shown that doping, in this case through diffusion, can result in lattice expansion and oxygen loss. In addition, strontium segregation and secondary phase formation has been shown in literature [12, 13, 14, 15] to occur under various operating conditions. Since the addition of sulfur into the LSV lattice is assumed to induce internal lattice strain and expansion, and the propensity of strontium to segregate into new phases, these two processes were viewed as the most likely modifications needed to the Rietveld refinement calculations for LSV.

Lattice expansion calculations can account for differences in atomic radii between sulfur and oxygen, assuming the induced strain caused by their volumetric differences will result in oxygen loss to alleviate the increased lattice strain. Sulfur has been reported to have an atomic radius

between 40-60% larger than oxygen [16, 17]. Using this crude approximation, the assumption that 40-60% of the oxygen loss from the room temperature material, accounted for by Rietveld analysis, was replaced by sulfur diffusion, could explain the emergence of monoclinic/tetragonal phases (i.e., typically oxygen rich phases, LaVO4) observed via XRD analysis in sub-samples with significant oxygen loss (i.e., 40-60% oxygen loss). The oxygen stoichiometry calculated in the Rietveld refinement was first multiplied by the percent oxygen loss, then that value was subtracted from the original oxygen stoichiometry of the material at room temperature to determine the reduced oxygen stoichiometry.

Strontium segregation/secondary phase formation calculations assume strontium diffusion/segregation from LSV forms strontium vanadate ($SrVO_3$). A crude approximation was also used to account for oxygen loss here, based on the experimental observance of strontium segregation and $SrVO_3$ phase formation in the LSV sub-samples taken at 700°C operating temperature. In all cases, at 700°C, samples had a cubic crystal structure. Since $SrVO_3$ has a cubic crystal structure, this analysis assumed the percentage oxygen loss would be equivalent to the percentage of the strontium vanadate phase present, since every crystal of $SrVO_3$ formed would destroy one crystal of LSV. Calculations first multiplied the percentage of $SrVO_3$ by the Rietveld oxygen stoichiometry and then subtracted that from the original Rietveld determined oxygen stoichiometry.

3.0 Experimental Results

3.1 Introduction

Although the experimental tests lasted for up to 100 hours, the following results will only focus on the sub-samples collected after the first 25 hours. This decision to limit analysis to the first 25 hours helps this paper limit the number of variables and isolate factors that influenced LSV sub-sample color. Future studies will investigate the impact time had on the results discovered in this research.

Color changes in the LSV sub-samples are hypothesized to be from oxidation number changes occurring in vanadium, assuming lanthanum prefers +3 oxidation state. Vanadium can have oxidation numbers of +5 (V_2O_5), +4 (VO_2), +3 (V_2O_3) and +2 (VO), while sample colors can range from a yellow/cream (+5, V_2O_5) to grey (+2, VO) [18], as shown in **Figure 5**. Untested LSV sub-samples have a yellow/cream color, as shown in **Figure 6**, and matches most closely to the +5 oxidation (V_2O_5) in **Figure 5**, however sample color is not as bright a yellow/cream color. This difference is hypothesized to be due to both lanthanum and strontium being present in LSV. Both lanthanum and strontium, when oxides, are nearly white in color, as shown in **Figure 7**. Since the vanadium oxide (V_2O_5) does not contain lanthanum or strontium it is hypothesized that the inclusion of these two elements reduces the +5 oxidation color intensity of V_2O_5.

As discussed above, there can be some variation in color between the reference vanadium oxide powder colors in **Figure 5** and the LSV sub-sample color, likely due to the inclusion of lanthanum and/or strontium. In addition, it is entirely possible that sub-samples could be a mixture of two or more different oxidation numbers, which would alter the sample color compared to an entirely single oxidation value. This, in turn, would suggest calculated fractional oxidation values are likely

the result of a mixture of different oxidation values, and not the result of one compound with a single fractional oxidation number, which can occur but is rare [19]. The exposed LSV sub-samples were observed to have colors ranging from brown, brownish blue, dark blue (nearly black) and black. The LSV sub-samples with a brown, brownish blue and dark blue color are not a clear match to any of the vanadium oxides (V_2O_5, VO_2, V_2O_3 or VO) shown in **Figure *4***, and probably contain multiple oxidation numbers mixed. The sub-samples that are black colors likely have oxidations numbers similar to the vanadium oxide (+3, V_2O_3), but still could have a range of values outside their traditional integer values. Oxidation number ranges were assigned, by the authors, based on visual observations of the LSV subs-samples.

Table 1 shows the range in average LSV sub-sample oxidation numbers and standard deviation for each color assigned by the authors. These values are used as a baseline to gauge whether the Rietveld refinement oxidation calculations are within reason.

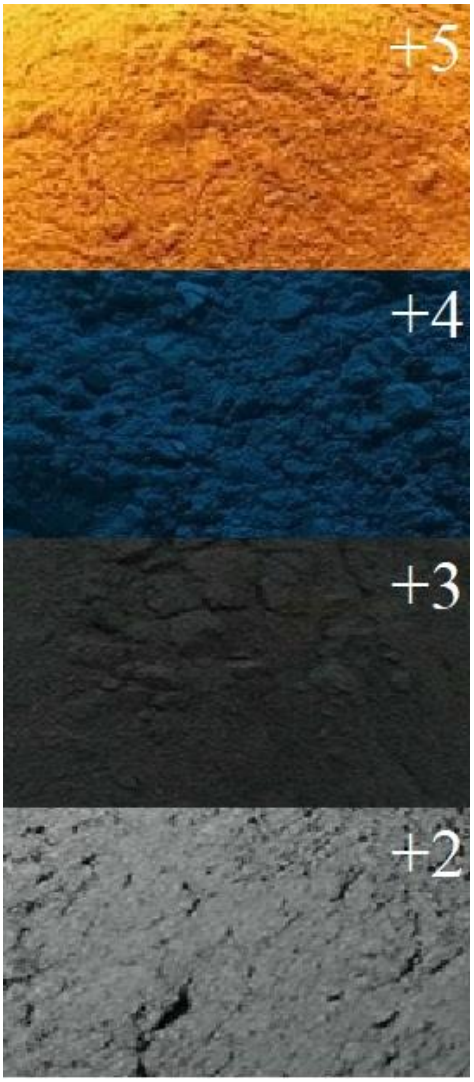

Figure 5: Optical Microscopy Images of Vanadium Oxide Colors and Oxidation Numbers

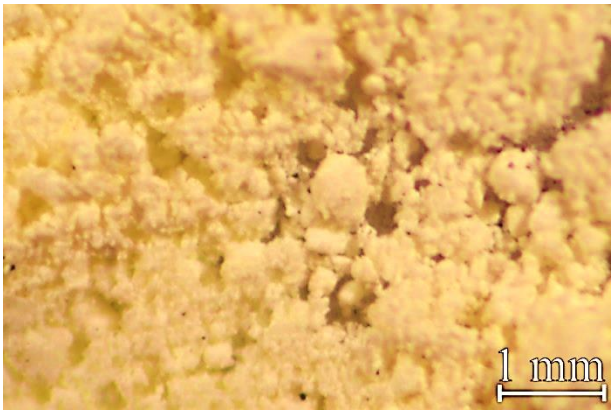

Figure 6: Optical Microscopy Image of Untested LSV

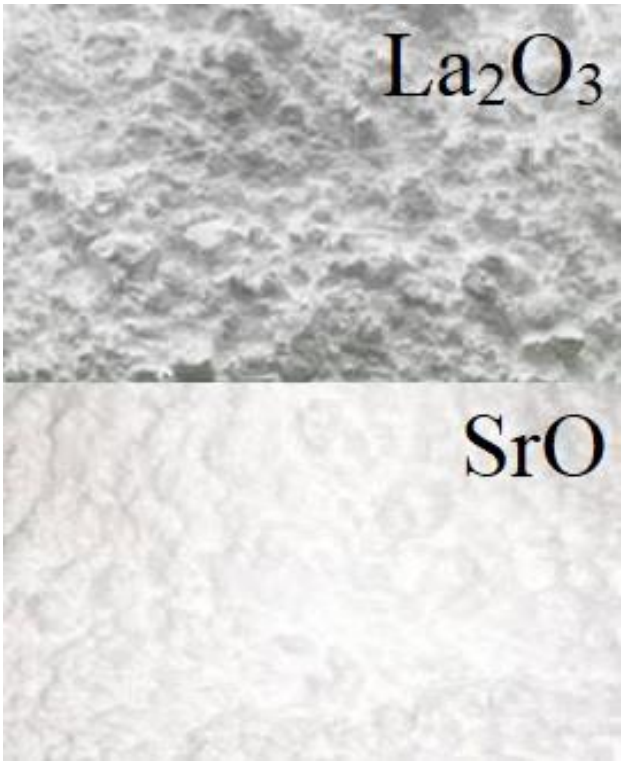

Figure 7: Optical Microscopy Images of Lanthanum Oxide (top) and Strontium Oxide (bottom)

Table 1: Oxidation Number Range

LSV Sample Color	Oxidation # Range	Average Oxidation #	Oxidation # SD
Brown	+5 to +4.5	+4.8	0.19
Brownish Blue	+4.3 to +3.7	+4.0	0.22
Dark Blue	+3.7 to +3.3	+3.5	0.16
Black	+3.2 to +2.8	+3.0	0.16

XRD spectra collected from exposed LSV sub-samples are shown in **Figure 8**, **Figure 9,** and **Figure 10**. Since the reference database did not contain LSV for peak identification, $LaVO_4$ and $LaVO_3$ were used instead and were observed to have a good match to experimental results. The $LaVO_4$ had a monoclinic phase and a tetragonal phase, as shown in **Figure 8**, that were both used for reference. $LaVO_3$ has been shown in literature to potentially have an orthorhombic [20, 21], polycrystalline [22], tetragonal [23] or cubic [24, 25] crystal structure. XRD scans of LSV sub-samples matched the closest to the cubic phase, as shown in **Figure 9**, which was used as a reference. LSV has 30% of its lanthanum replaced with strontium which has been shown to promote the cubic phase over the other phases [26, 23]. The use of cubic $LaVO_3$ to represent LSV may be appropriate currently (25 hours), LSV could revert to a more orthorhombic/tetragonal structure if enough strontium segregated over a much longer duration. Untested LSV powder contained the monoclinic and tetragonal phases, which were observed to be present at lower operating temperatures. LSV sub-samples matched the $LaVO_3$ cubic reference phase near the upper range of testing temperatures. One additional phase, $SrVO_3$, was also observed at 700°C, which presented itself as a side peak next to the cubic phase, as shown in **Figure 10**.

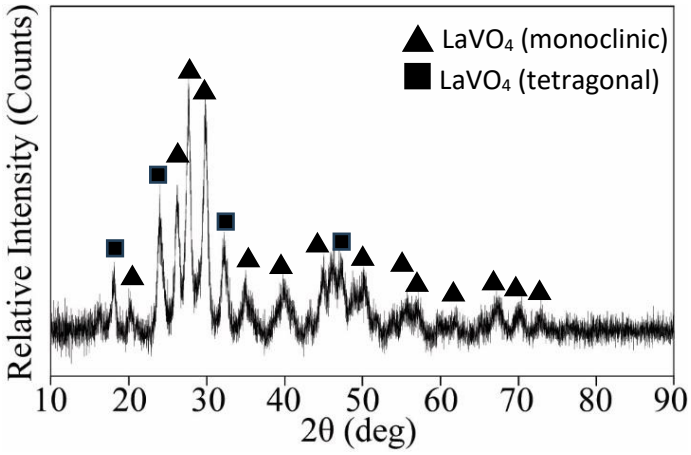

Figure 8: Monoclinic and Tetragonal $LaVO_4$ Phase XRD Spectra for LSV. ▲$LaVO_4$ (monoclinic) and ■ $LaVO_4$ (tetragonal).

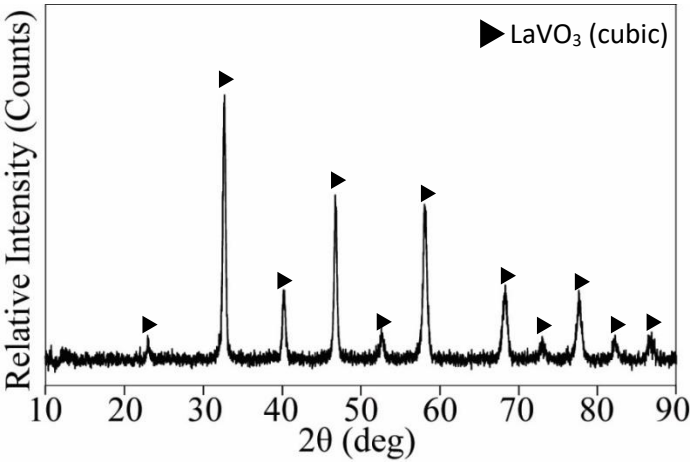

Figure 9: Cubic $LaVO_3$ Phase XRD Spectra for LSV. ►$LaVO_3$ (cubic)

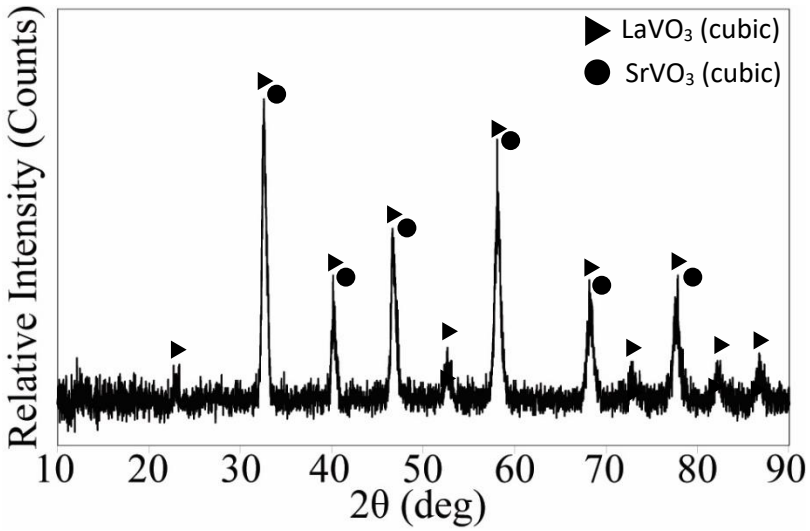

Figure 10: Cubic $LaVO_3$ and Cubic $SrVO_3$ Phase XRD Spectra for LSV at 700°C. ▶ $LaVO_3$ (cubic) and ● $SrVO_3$ (cubic).

3.2 Hydrogen Gas Experimental Results

Table 2 lists the LSV sub-sample optical microscopy powder colors and XRD crystal phases present after heated exposure for 25 hours to 300ppm H_2S balance H_2 gas, followed by the raw experimental results.

Table 2: LSV Sub-Samples Heated in 300ppm H_2S Balance H_2 Gas Properties

Operating Temperature (°C)	LSV Sample Color	Crystal Phases
400	Brown	$LaVO_4$ (monoclinic), $LaVO_4$ (tetragonal)
500	Brown	$LaVO_4$ (monoclinic), $LaVO_4$ (tetragonal)
600	Black	$LaVO_3$ (cubic)
700	Black	$LaVO_3$ (cubic)

Figure 11 shows optical microscopy images of LSV sub-samples after being heated between 400-700°C for 25 hours with exposure to 300ppm H_2S balance H_2 gas. Sub-sample colors were observed to be brown between 400-500°C and then switch to black between 600-700°C. The LSV samples switched between brown and black between 500°C and 600°C, where they were also observed to change from the monoclinic and tetragonal crystal phase mixture to the cubic phase as detailed in the following **Figure 12**.

Figure 12 shows the XRD spectra of LSV sub-samples after being heated between 400-700°C for 25 hours with exposure to 300ppm H_2S balance H_2 gas. LSV maintained a mixture of the monoclinic and tetragonal phases between 400-500°C, but then transitioned to a cubic phase at 600°C and remained till 700°C.

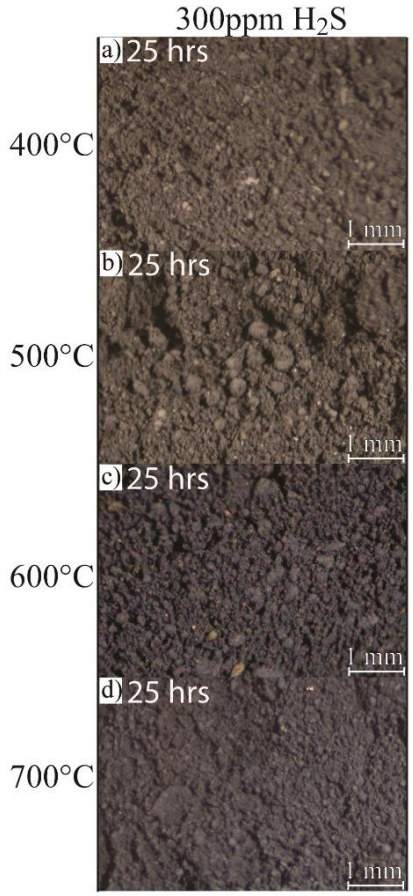

Figure 11: Optical Microscopy Images of LSV Sub-Samples Heated at a) 400°C, b) 500°C, c) 600°C and d) 700°C for 25 Hours in 300ppm H_2S Balance H_2 Gas.

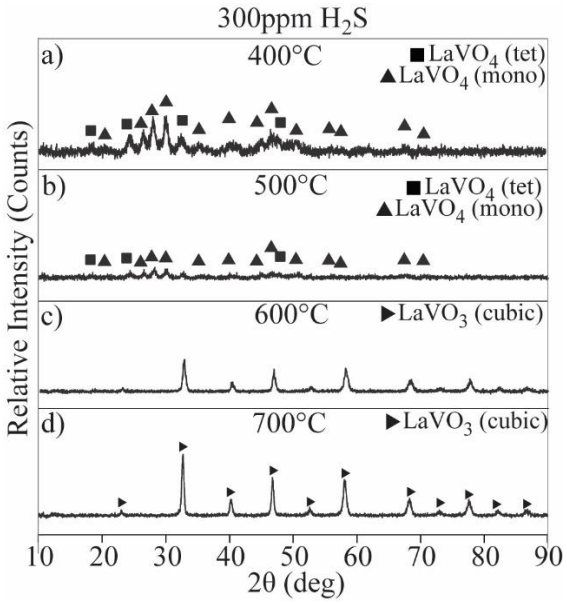

Figure 12: XRD Spectra of LSV Sub-Samples Heated at a) 400°C, b) 500°C, c) 600°C and d) 700°C for 25 Hours in 300ppm H_2S Balance H_2 Gas.

Table 3 shows the previously reported average adsorption rates and standard deviations for LSV sub-samples heated between 400-700°C with exposure to 300ppm H_2S balance H_2 gas. As previously reported, adsorption rates are significantly higher at the lower operating temperatures, which contained the monoclinic and tetragonal phases, and was observed to drastically drop once the cubic phase is formed at 600°C.

Table 3: Hydrogen LSV Sub-Sample Sulfur Adsorption Rates

Operating Temperature (°C)	Average Sulfur Adsorption Rate (ng S/(um^2*hr)	Adsorption Rate SD
400	0.01516	0.00088
500	0.01300	0.00032
600	0.00576	0.00076
700	0.00332	0.00020

3.3 Methane Gas Experimental Results

Table 4 lists the LSV sub-sample optical microscopy powder colors and XRD crystal phases present after being heated for 25 hours with exposure to 300ppm H_2S balance CH_4 gas. The raw experimental results are shown in **Figure 13 and 14**.

Table 4: LSV Sub-Samples Heated in 300ppm H_2S Balance CH_4 Gas Properties

Operating Temperature (°C)	LSV Sample Color	Crystal Phases
400	Brown	$LaVO_4$ (monoclinic), $LaVO_4$ (tetragonal)
500	Brown	$LaVO_4$ (monoclinic), $LaVO_4$ (tetragonal)
600	Brownish Blue	$LaVO_4$ (monoclinic), $LaVO_4$ (tetragonal), $LaVO_3$ (cubic)
700	Black	$LaVO_3$ (cubic), $SrVO_3$ (cubic)

Figure 13 shows optical microscopy images of LSV sub-samples after being heated between 400-700°C for 25 hours with exposure to 300ppm H_2S balance CH_4 gas. Similar to the sub-samples tested using H_2 gas, these sample colors are also brown between 400-500°C, while the 600°C sub-sample contained a majority of blue coloring, with a small amount of brown coloring in it. Finally, the 700°C was observed to have a black color, as was observed with the H_2 samples. These LSV samples appeared to switch between brown and black at a slightly higher operating temperature, estimated to be between 630-650°C. The crystal structure, detailed in **Figure 14**, was observed to switch between the monoclinic/tetragonal phases and the cubic phase between 600°C and 700°C as with sample powder colors. The operating temperature where LSV sub-samples transitioned from a monoclinic/tetragonal phase to a cubic phase is also estimated to be between 630-650°C.

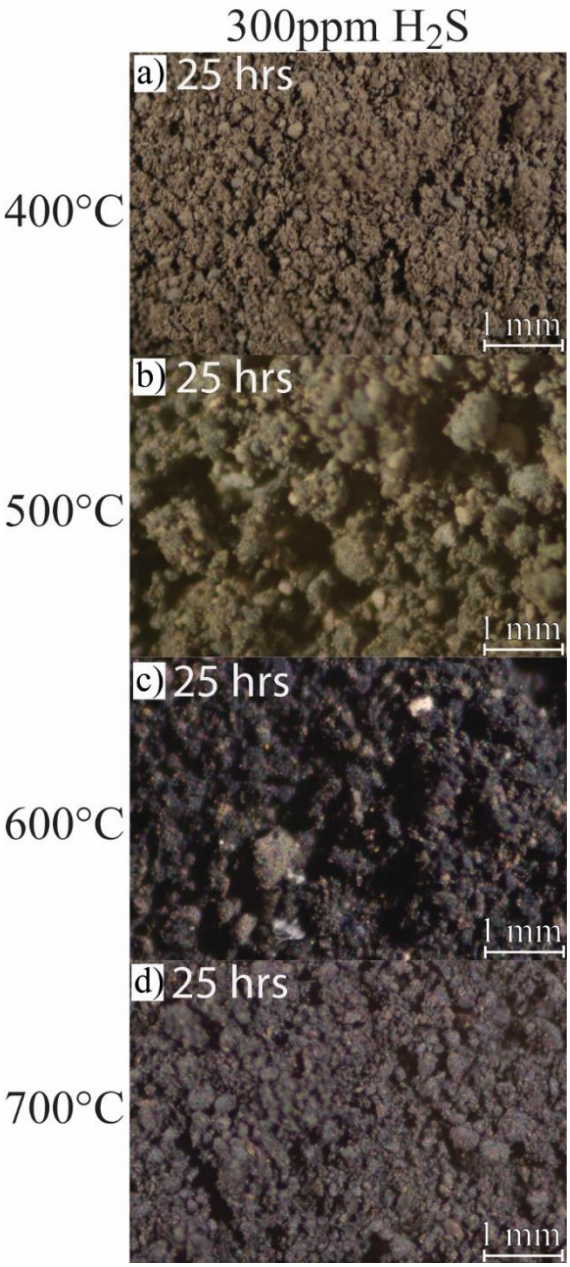

Figure 13: Optical Microscopy Images of LSV Sub-Samples Heated at a) 400°C, b) 500°C, c) 600°C and d) 700°C for 25 Hours in 300ppm H_2S Balance CH_4 Gas.

Figure 14 shows the XRD spectra of LSV sub-samples after being heated between 400-700°C for 25 hours with exposure to 300ppm H_2S balance CH_4 gas. As with the H_2 sub-samples, the LSV maintained a mixture of the monoclinic/tetragonal phases between 400-500°C, but unlike the H_2 sub-sample, also exhibited a small percentage of the monoclinic/tetragonal phases at 600°C. This correlates with the brown color observed with the optical microscopy images, shown in **Figure 13**, and additionally demonstrates the phase transition to cubic is elevated with exposure to CH_4 gas when compared to the H_2 sub-samples. Finally, the cubic phase is the dominant phase at 600°C and above.

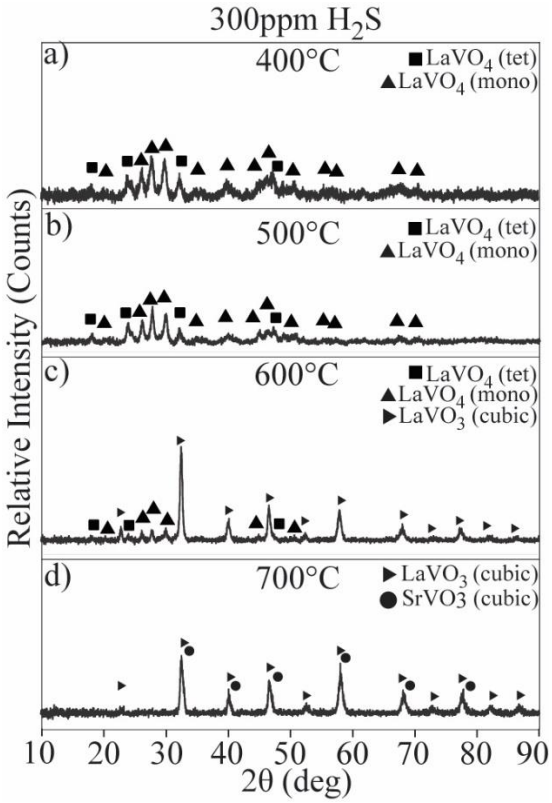

Figure 14: XRD Spectra of LSV Sub-Samples Heated at a) 400°C, b) 500°C, c) 600°C and d) 700°C for 25 Hours in 300ppm H_2S Balance CH_4 Gas.

Table 5 shows the previously reported average adsorption rates and standard deviations for LSV sub-samples heated between 400-700°C with exposure to 300ppm H_2S balance CH_4 gas. The methane results are similar to the previous hydrogen results, with significantly higher adsorption rates when the monoclinic and tetragonal phases are present. However, the transition to the cubic phase only starts at 600°C, which correlates to the elevated adsorption rate observed over hydrogen results, until it decreases at 700°C, where there is a $SrVO_3$ phase also present likely due to strontium segregation.

Table 5: Methane LSV Sub-Sample Sulfur Adsorption Rates

Operating Temperature (°C)	Average Sulfur Adsorption Rate (ng S/(um^2*hr)	Adsorption Rate SD
400	0.00976	0.00124
500	0.01812	0.00152
600	0.03036	0.00504
700	0.00896	0.00116

3.4 Methanol Solution Experimental Results

Table 6 lists the LSV sub-sample optical microscopy powder colors and XRD crystal phases present after being heated for 25 hours with exposure to 300ppm C_4H_4S balance CH_3OH solution. The raw experimental results are shown in **Figure 15 and 16**.

Table 6: LSV Sub-Samples Heated in 300ppm C_4H_4S Balance CH_3OH Solution Properties

Operating Temperature (°C)	LSV Sample Color	Crystal Phases
400	Black	$LaVO_4$ (monoclinic), $LaVO_4$ (tetragonal)
500	Black	$LaVO_4$ (monoclinic), $LaVO_4$ (tetragonal)
600	Black	$LaVO_4$ (monoclinic), $LaVO_4$ (tetragonal)
700	Black	$LaVO_3$ (cubic), $SrVO_3$ (cubic)

Figure 15 shows optical microscopy images of LSV sub-samples after being heated between 400-700°C for 25 hours with exposure to 300ppm C_4H_4S balance CH_3OH solution. Unlike the previous two exposure fuel regimes, the sub-sample color was not observed to contain brown coloring at lower operating temperatures and all sub-samples were observed to be black or very dark blue in color. This initially suggested that the sub-sample phases may be cubic at lower operating temperatures, but as shown in **Figure 16**, the monoclinic and tetragonal phases were still very much present.

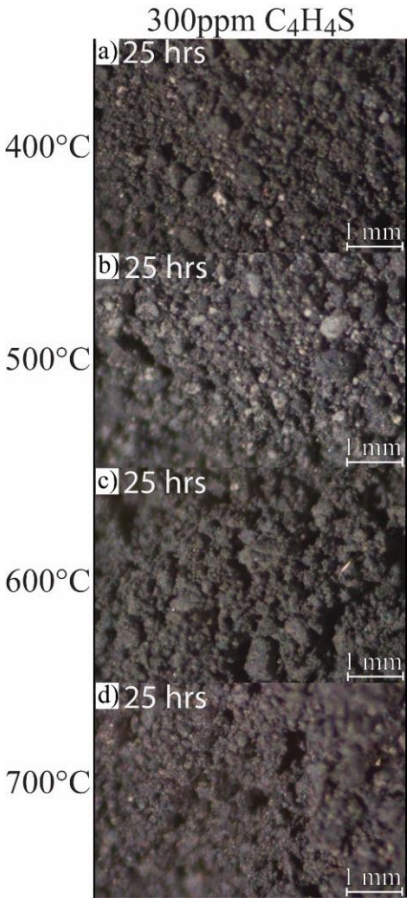

Figure 15: Optical Microscopy Images of LSV Sub-Samples Heated at a) 400°C, b) 500°C, c) 600°C and d) 700°C for 25 Hours in 300ppm C_4H_4S Balance CH_3OH Solution.

Figure 16 shows the XRD spectra of LSV sub-samples after being heated between 400-700°C for 25 hours with exposure to 300ppm C_4H_4S balance CH_3OH solution. The XRD results are closer to the methane results than the hydrogen, as the monoclinic and tetragonal phases were again observed to be present at 600°C. Strontium vanadate was also observed to be present at 700°C, although the side peak is minimal. As mentioned previously, the sample colors observed when using methanol did not result in the expected crystal phases. Possible reasons for this difference will be discussed in the Section 4.0 of this paper.

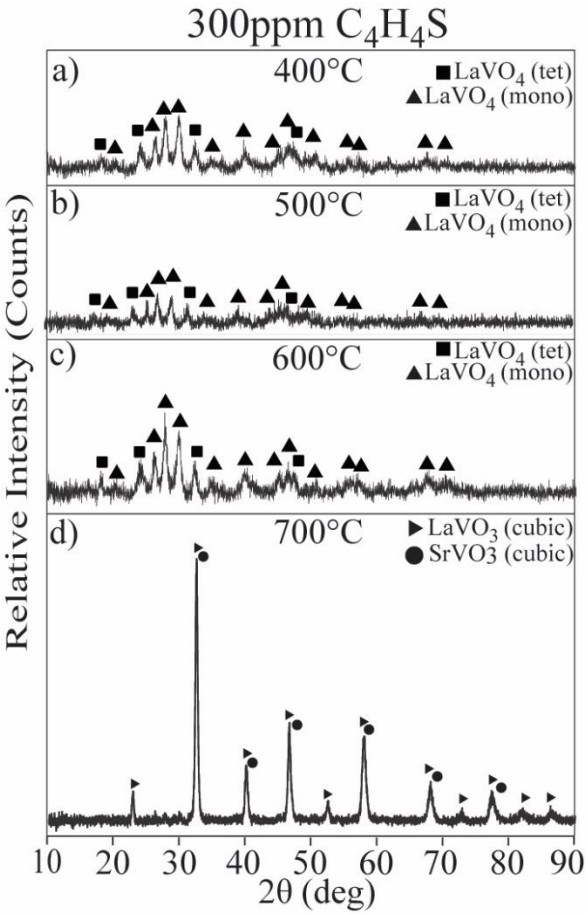

Figure 16: XRD Spectra of LSV Sub-Samples Heated at a) 400°C, b) 500°C, c) 600°C and d) 700°C for 25 Hours in 300ppm C_4H_4S Balance CH_3OH Solution.

Table 7 shows the previously reported average adsorption rates and standard deviations for LSV sub-samples heated between 400-700°C with exposure to 300ppm C_4H_4S balance CH_3OH solution. In these sub-samples, the adsorption results are not similar any of the hydrogen or methane experimental results. There was significantly lower sulfur adsorption present at all operational temperatures. These sulfur adsorption rates with methanol were observed to be 76% to 96% lower than the hydrogen sulfur adsorption rates. This significant difference in sulfur adsorption will also be discussed in greater detail in Section 4.0.

Table 7: Methanol LSV Sub-Sample Sulfur Adsorption Rates

Operating Temperature (°C)	Average Sulfur Adsorption Rate (ng S/(um^2*hr)	Adsorption Rate SD
400	0.00064	0.00056
500	0.00112	0.00204
600	0.00136	0.00204
700	0.00048	0.00048

4.0 Rietveld Refinement Results and Discussions

4.1 Introduction

To understand the trends observed in the experimental data, Rietveld refinement analyses were performed on the XRD spectra to calculate the oxygen stoichiometry in each sample. The oxygen stoichiometry was then used to determine the vanadium oxidation number for each sub-sample. Ideally, the calculated vanadium oxidation number should be close to the predicted oxidation number determined from its color when compared to vanadium oxide references. Samples from each balance gas (H_2 or CH_4) or balance solution (CH_3OH) were analyzed independently to help isolate trends.

4.2 Hydrogen Gas Rietveld Refinement and Discussions

Figure 17 shows vanadium oxidation and oxygen stoichiometry values for LSV sub-samples heated between 400-700°C with exposure to 300ppm H_2S balance H_2 gas. From these results, there appeared to be two different vanadium oxidation values, as detailed with bars with and without black outlines, determined using the following approaches. Values depicted without black outlines were calculated by comparing the LSV sub-sample colors to the vanadium oxide reference colors (**Figure *5***) and then assigned vanadium oxidation values. This assumes vanadium is the dominant contributor to sample, which as shown earlier, is influenced by lanthanum and strontium too. Despite the addition of lanthanum and strontium, the authors feel the assumption vanadium is the dominant contributor is still a realistic approximation, since previously shown results (**Figure *6***) were different in color saturation only and not in color variation. Values with black outlines are calculated using the oxygen stoichiometry determined using the Rietveld refinement. The oxygen stoichiometry values are either directly reported from the Rietveld refinement calculations or modified Rietveld oxygen stoichiometry considering oxygen loss from lattice expansion or strontium segregation.

Initially, the ideal oxidation number based around the LSV sample color (obtained by optical characterization), compared to vanadium oxide samples shown in **Figure *5***, would be between +4.75 and +3. However, the Rietveld calculated LSV vanadium oxidation values are significantly lower between +2.46 and 0. If the latter is correct, then sample colors would be black or grey (at least between 400-500°C), and/or the vanadium would be reverted to its pure metal state (0 oxidation state) and would have been present in the XRD spectra. Neither was observed, so additional processes must be occurring to raise the vanadium oxidation value.

This leads the authors to conclude that the increase in oxidation state could be in the inclusion of an additional element into the oxygen deficiencies within the LSV lattice. Strontium segregation in the form of strontium vanadate is not observed in the XRD spectra of lower temperature sub-samples, however in light of the LSV sub-samples being exposed to sulfur (in the form of H_2S), it is hypothesized that sulfur diffusion into the LSV lattice, could account for the increase in vanadium oxidation state. Looking at H_2S the oxidation state of sulfur would be -2 since the oxidation state of hydrogen is +1. Sulfur was included in the vanadium oxidation calculations, assuming its oxidation state remained -2, using **Equations 7-9**.

The stoichiometry of sulfur atoms used in **Equations 7-9** were adjusted to increase the LSV vanadium oxidation number to as close as possible to the ideal vanadium oxide calculations, while also trying to maintain the same sulfur ratios observed in the experimental results in **Table 3**.

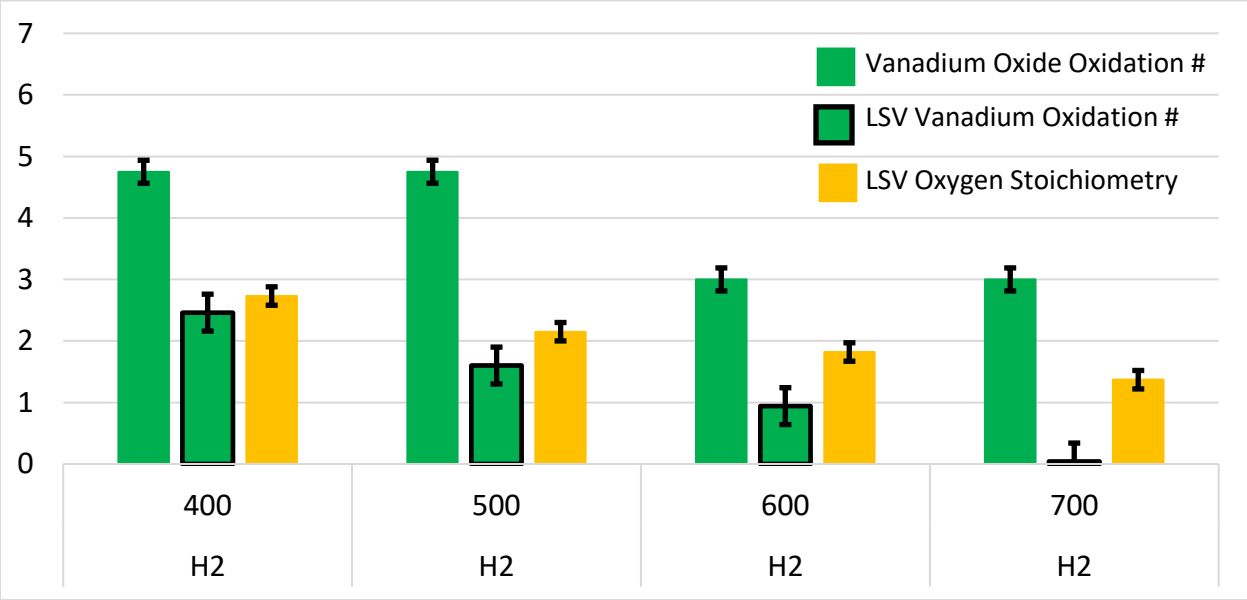

Figure 17: Hydrogen Gas Calculated Oxygen Stoichiometry and Vanadium Oxidation Number from Rietveld Refinements on LSV Samples Heated Between 400-700°C.

Figure 18 shows the updated vanadium oxidation numbers after accounting for the addition of sulfur to the LSV lattice structure. All the updated values are statistically similar to their vanadium oxide reference counterpart estimations. The differences in averages observed could be accounted for based on the fact that the vanadium oxidation state from vanadium oxide is an estimate based on visual observations which can vary from person to person, as well as the inclusion of lanthanum and strontium. These color differences would also introduce some error into the comparison. Lastly, the Rietveld refinement is only as accurate as XRD spectra used. There may be additional phases present in the LSV powder, which are too small to identify using the XRD reference database which could influence results.

Table 8 shows the number of sulfur atoms used to calculate the LSV vanadium oxidation numbers in **Figure 18**. The differences between these values and the experimental sulfur adsorption values shown in **Table 3** are close, but specifically the number of sulfur atoms at 400°C is lower than at

500°C, while the adsorption rate results progressively decrease from 400-700°C. The reason for this small difference is not presently clear, but is hypothesized to be caused by additional unaccounted for phases in the XRD results too small to identify.

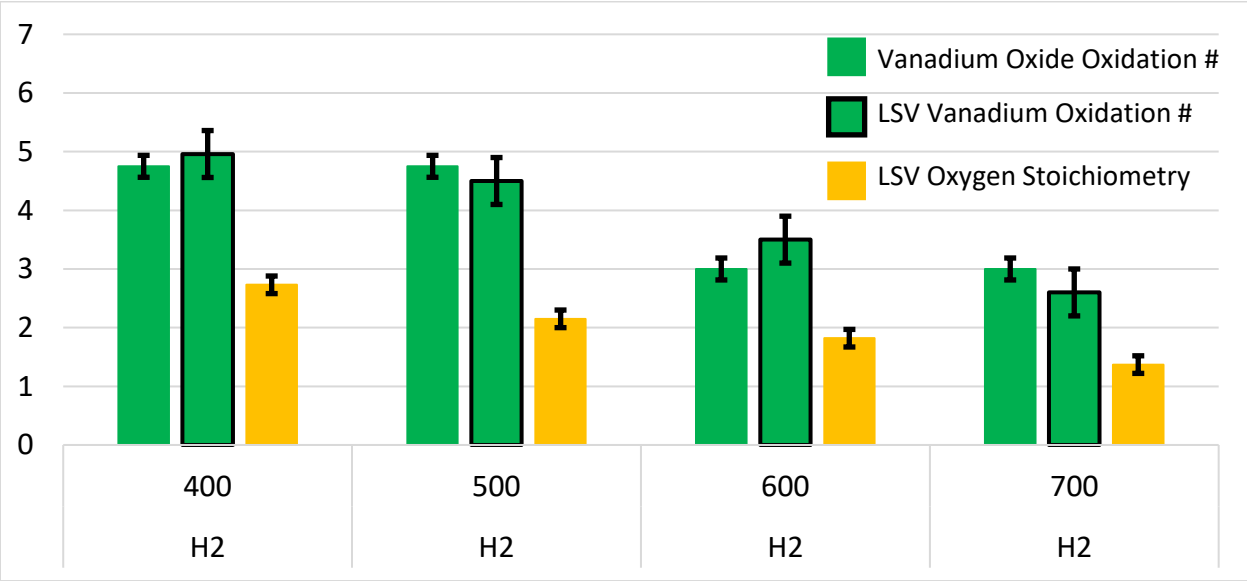

Figure 18: Sulfur Diffusion Updated Hydrogen Gas Calculated Oxygen Stoichiometry and Vanadium Oxidation Number from Rietveld Refinements on LSV Samples Heated Between 400-700°C.

Table 8: Hydrogen LSV Sulfur Addition for Rietveld Refinement

Operating Temperature (°C)	Sulfur Atom Addition
400	1.10
500	1.45
600	1.30
700	1.26

4.3 Methane Gas Rietveld Refinement and Discussions

Figure 19 shows vanadium oxidation and oxygen stoichiometry values for LSV sub-samples heated between 400-700°C with exposure to 300ppm H_2S balance CH_4 gas. All three values are calculated in the same manner as with the hydrogen results shown above.

Similar to the hydrogen results the ideal oxidation number would be between +4.75 and +3, however the 600°C result is +4 here instead of +3. Here the Rietveld calculated LSV vanadium oxidation values do not match the ideal values, but are closer, between +2.60 and +2.24. The calculated vanadium oxidation states are 5.38% and 98% higher than previously observed with hydrogen, which are hypothesized to be from the increased oxygen stoichiometry content. As with the previous hydrogen gas calculations, factoring in sulfur adsorption is a good first step to increase the calculated LSV vanadium oxidation values to match the ideal case. The effects of oxygen stoichiometry will be looked at next if the sulfur does not produce adequate results.

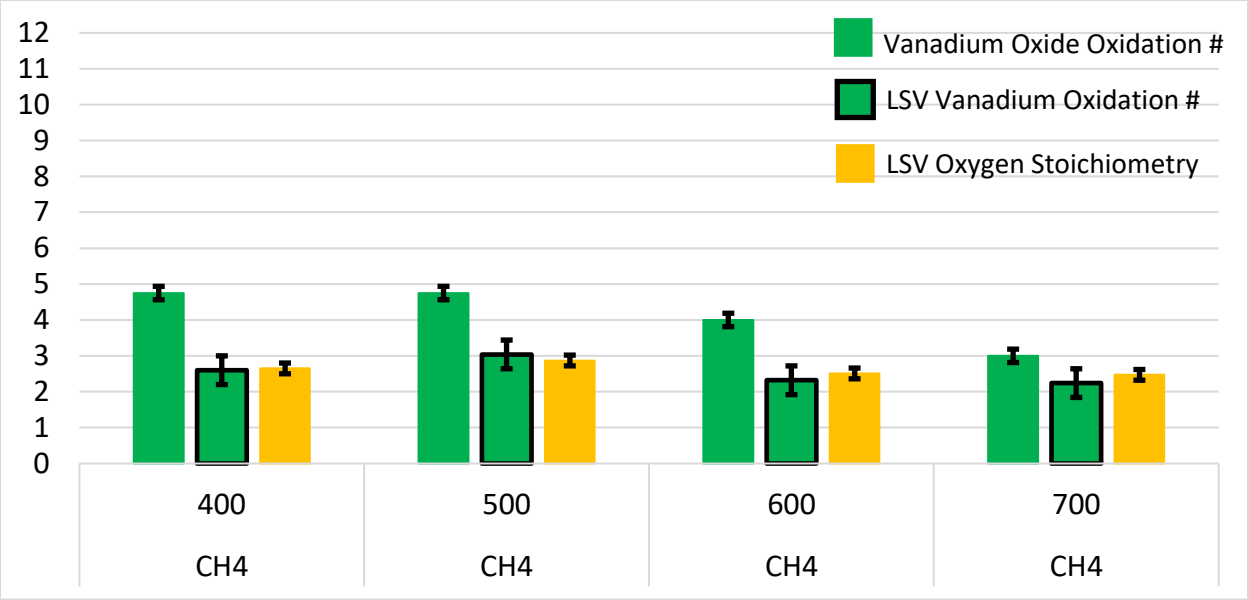

Figure 19: Methane Gas Calculated Oxygen Stoichiometry and Vanadium Oxidation Number from Rietveld Refinements on LSV Samples Heated Between 400-700°C.

Figure 20 shows the updated vanadium oxidation numbers after accounting for the addition of sulfur to the LSV lattice structure. The increased oxygen stoichiometry and slightly higher ideal vanadium oxidation values contribute this time to significantly elevated Rietveld calculated vanadium oxidation numbers. One rational response would be to lower the amount of sulfur added, such that the two vanadium oxidation values match. The problem with that rationale is that the amount of sulfur atoms added needs to be similar to the trends observed with the adsorption rates reported earlier. The adsorption rates between 500-700°C using methane are higher than that of hydrogen, which results in the values shown in **Figure 20**.

Table 9 shows the range in ratio values between methane and hydrogen if the adsorption rates in **Table 5** (methane) were divided by the adsorption rates in **Table 3** (hydrogen). The adsorption rate (high) value is the largest possible ratio determined by dividing the largest CH_4 adsorption rate by the smallest H_2 adsorption rate. The adsorption rate (low) is determined in the same manner but by using the largest CH_4 and smallest H_2 adsorption rate values instead.

Table 10 shows the number of sulfur atoms used to calculate the LSV vanadium oxidation numbers in **Figure 20** and the actual CH_4/H_2 sulfur atomic ratio. Samples at lower operating temperatures have had their sulfur atomic ratios set within the range established in **Table 9**. Samples with higher operating temperatures had the sulfur atomic ratios lower than in **Table 9**. The amount of sulfur could not simply be raised further, so the ratio fell within the range established in **Table 9**. As shown in **Figure 21**, the vanadium oxidation numbers at 600°C and 700°C would be increased to such an extreme that no amount of oxygen loss could reduce them back to match the vanadium oxidation values for their respective powder colors. The following hypothesis could account for the discrepancy in sulfur content between the Rietveld sulfur content and the experimental sulfur adsorption rates. The experimental adsorption rates were determined

using EDS, which measures sulfur within the lattice, but also on the surface of the LSV sample particles. The increased sulfur content using methane may have been more distributed on the surface of the LSV sub-samples, which would increase the total adsorption rate, but the Rietveld calculations presented in this paper do not account for that.

Since the sulfur content cannot be adjusted further, the only plausible explanation for the reduced vanadium oxidation values to match the ideal case would be to reduce the oxygen stoichiometry values. Two methods, which were not included in the original Rietveld refinement, are oxygen loss through lattice expansion and/or strontium vanadate formation through strontium segregation.

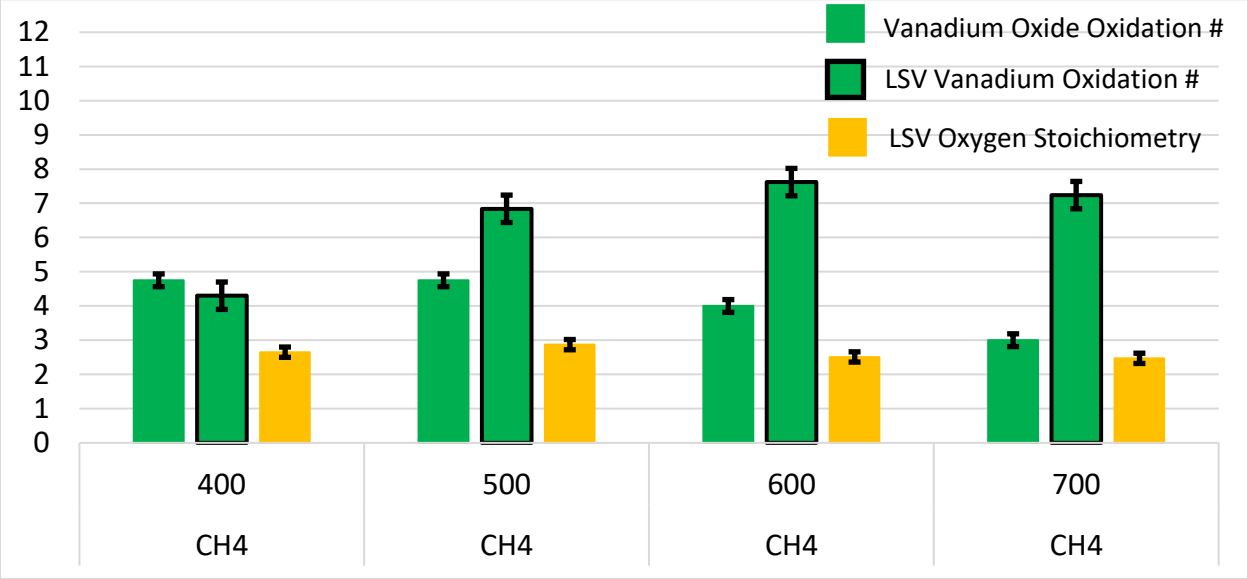

Figure 20: Sulfur Diffusion Updated Methane Gas Calculated Oxygen Stoichiometry and Vanadium Oxidation Number from Rietveld Refinements on LSV Samples Heated Between 400-700°C.

Table 9: Methane/Hydrogen Gas Adsorption Rate Ratio Range

Operating Temperature (°C)	CH_4/H_2 Sulfur Adsorption Rate Ratio (High)	CH_4/H_2 Sulfur Adsorption Rate Ratio (Low)
400	0.8	0.5
500	1.6	1.2
600	7.1	3.9
700	3.2	2.2

Table 10: Methane LSV Sulfur Addition for Rietveld Refinement

Operating Temperature (°C)	Sulfur Atom Addition	CH_4/H_2 Sulfur Atom Ratio
400	0.85	0.8
500	2.10	1.4
600	2.65	2.1
700	2.50	2.0

Figure 21 shows the updated LSV vanadium oxidation values back calculated after accounting for oxygen loss through lattice expansion and strontium vanadate formation. For these final adjustments the 500-700°C calculations assumed the increased adsorption of sulfur atom induced lattice strain. A 50% oxygen loss, due to lattice strain, was used for the 500°C calculations and a 65% oxygen loss was used for both the 600-700°C calculations. In addition, the 700°C calculation assumed a 20% oxygen loss to $SrVO_3$ formation. All oxygen loss calculations were performed using the approaches outlined in Section 2.4.4.

After performing these final adjustments to the Rietveld refinement, the LSV vanadium oxidation numbers are statistically similar to the ideal values. The oxygen stoichiometry values are also significantly lower, especially at higher operating temperatures, than the final calculated hydrogen oxygen stoichiometry values, which coincides with increased sulfur adsorption observed.

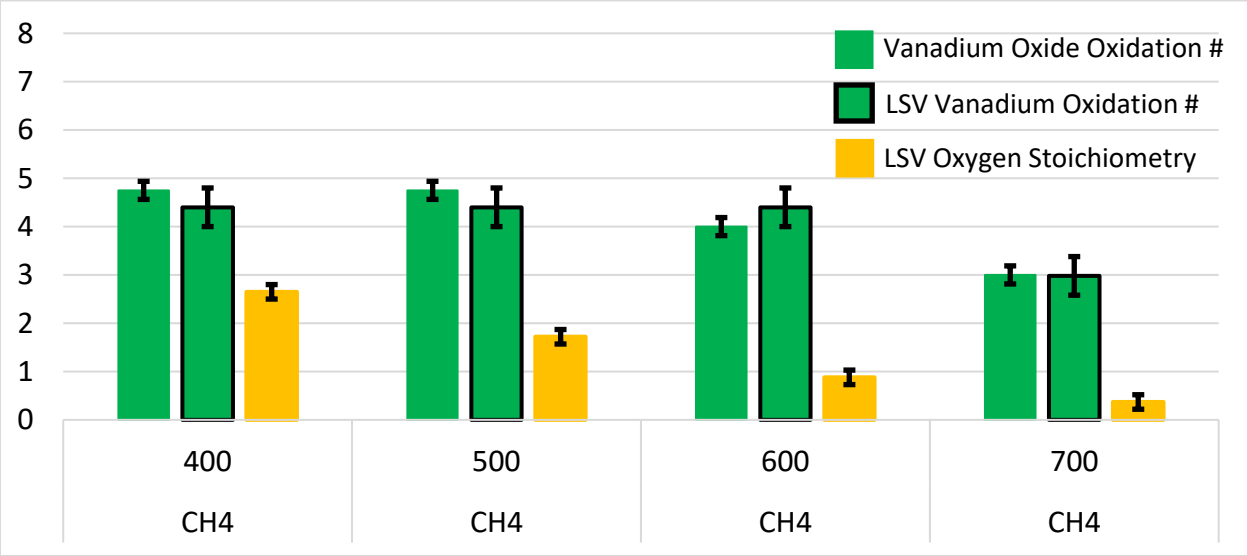

Figure 21: Sulfur Diffusion/Oxygen Loss Updated Methane Gas Calculated Oxygen Stoichiometry and Vanadium Oxidation Number from Rietveld Refinements on LSV Samples Heated Between 400-700°C.

4.4 Methanol Solution Rietveld Refinement and Discussions

Figure 22 shows vanadium oxidation and oxygen stoichiometry values for LSV sub-samples heated between 400-700°C with exposure to 300ppm C_4H_4S balance CH_3OH solution. All three values are calculated in the same manner as with the hydrogen or methane results shown previously.

The methanol sub-samples were observed to be experimentally different from the hydrogen and methane sub-samples. The following calculations, performed on methanol samples, produced very different results compared to the hydrogen and methane calculations. First, the vanadium oxide oxidation values calculated by optical comparing colors (bar without black outlines) are much lower between 400-700°C. Those optically determined vanadium oxidation values for methanol vary between +3.5 and +3, which are lower than the +4.75 to +3 seen previously with hydrogen and methane. Second, the Rietveld refinement oxygen stoichiometries are generally consistent

around 3.0, which is a larger value, on average, between 400-700°C compared to the hydrogen and methane sub-samples after the initial Rietveld refinement. Due to this consistent and increased oxygen stoichiometry (compared to the hydrogen and methane samples) the initial Rietveld calculated LSV vanadium oxidation values statistically match the ideal values from the start.

This consistency between the LSV vanadium oxidation values and the ideal values is primarily, in this authors viewpoint, due to the lack of sulfur adsorption. **Table 7** showed that the methanol adsorption rates were 76% to 96% lower than hydrogen and 93% to 96% lower than methane. One update to these calculations that could be included, but would not influence the outcome, is the inclusion of oxygen loss from $SrVO_3$ formation at 700°C. The $SrVO_3$ phase fraction is only approximately 6%, but would reduce the LSV vanadium oxidation value by 0.3 (from +3.1 to +2.8), which is still statistically similar to the ideal case.

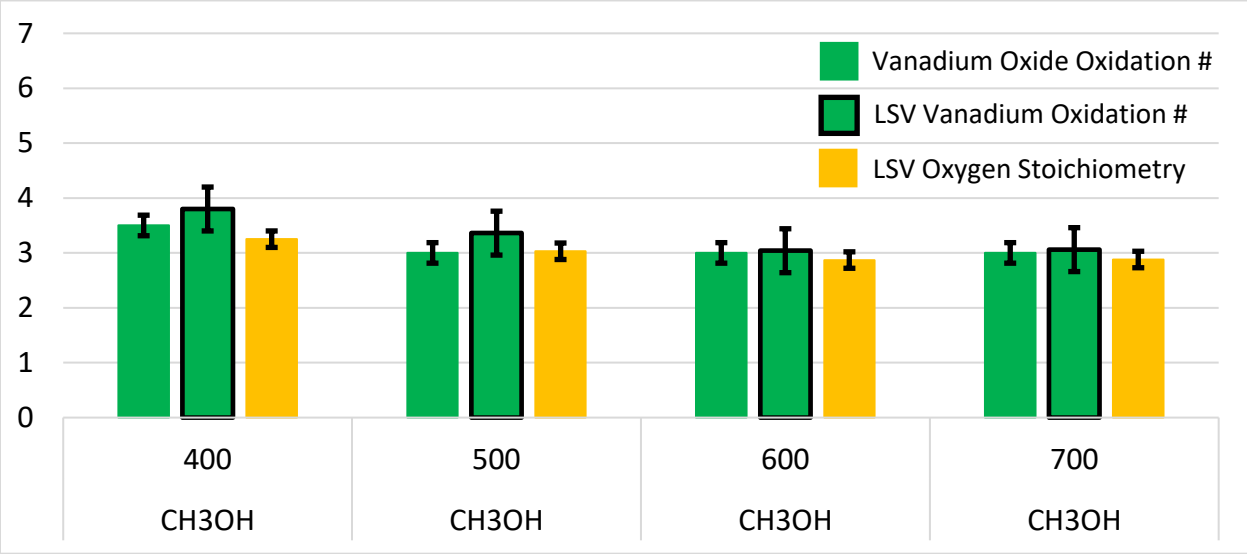

Figure 22: Methanol Solution Calculated Oxygen Stoichiometry and Vanadium Oxidation Number from Rietveld Refinements on LSV Samples Heated Between 400-700°C.

The fact the methanol LSV sub-samples matches the ideal scenario without any adjustments to the Rietveld refinement is very unusual compared to the hydrogen and methane LSV sub-samples. This difference is viewed as a result of the low sulfur adsorption. The LSV crystal phases are similar between the methanol, methane and hydrogen samples, so that would be an unlikely contributor to low sulfur. A second consideration is that the sulfur compound used with methanol, C_4H_4S, contains a ring structure, which H_2S does not have. The sulfur is also placed between two carbon atoms instead of two hydrogen atoms. These structural differences between C_4H_4S and H_2S may contribute to lower sulfur reactivity. This hypothesis also lacks much standing since literature has shown thiophene can become reactive with vanadium oxide [27, 28] vanadium metal [29] and lanthanum oxide [30] as soon as 400°C. All operating temperatures used in this paper were at or above 400°C, so it is unlikely thiophene is unreactive itself. While these structures are different from LSV, their elemental constituents are contained within LSV, especially vanadium and lanthanum. These similarities along with thiophene's demonstrated reactivity, makes this second hypothesis likely invalid for being the primary contributor for low sulfur adsorption. One

final rationale could be the balance gas/solution used as methanol is a liquid (instead of a gas), as well as polar. The differences in states of matter (liquid and gas) between H_2, CH_4 and CH_3OH is irrelevant since CH_3OH enters the reactor as a liquid and then rapidly changes into a gas (due to the operating temperature being above its boiling point) before interaction with the LSV material. The polarity between the different compounds may be a contributing factor. Literature has shown methanol has an affinity with vanadium oxide [31, 32, 33, 34], lanthanum oxide [35] and lanthanum doped perovskite [36] materials. Just like with thiophenes reactivity, the material analyzed in these literatures' studies are close to LSV or contain constituents within LSV, which indicates this same or similar reactivity would carry over to LSV as well. One final point to mention is that earlier in this paper the thermal decomposition temperature of methanol was reported to be around 700°C, which was speculated to potentially influence results. This does not appear to be the case as **Table *7*** does not show any increased sulfur adsorption trends around 700°C. There are few explanations that could account for this discrepancy. First, the thermal decomposition of methanol may be a slow process around 700°C, since that is the initial temperature decomposition begins, so any effects may not be seen until more time has passed. Second, the ratio of methanol to thiophene is high enough, when using only 300ppm of thiophene, that any methanol decomposition may never be noticed.

After analyzing the differences between the sub-samples, experimented using 300ppm H_2S in hydrogen, 300ppm H_2S in methane and 300ppm C_4H_4S in methanol, the observed decrease in sulfur adsorption with methanol is most likely the result of interactions between methanol and LSV. It is hypothesized the affinity between methanol and LSV is greater than between thiophene and LSV, thus blocking the reaction sites where sulfur or sulfur compounds would react.

5.0 Conclusions

This paper analyzed the Rietveld calculated LSV vanadium oxidation number and compared those calculations to the expected vanadium oxidation values based on sample visual observations. This analysis was performed on samples exposed to H_2S in hydrogen gas, H_2S in methane gas and C_4H_4S in liquid methanol. Initial calculated vanadium oxidation values, determined using Rietveld oxygen stoichiometries, did not consistently match the expected oxidation values determined by LSV visual characterization and comparison to vanadium oxide reference samples. Initial Rietveld calculations were adjusted to account for sulfur diffusion into the lattice and lattice oxygen loss through strain and strontium segregation/secondary phase formation. Making these adjustments to the Rietveld calculations improved accuracy of the LSV vanadium oxidation values so they were statistically similar to vanadium oxidation values determined using visual characterization.

This analysis elucidates a few important points that help explain the observed experimental results. First, the inclusion of sulfur (at least at 300ppm concentration) can result in the vanadium oxidation value being increased. Increasing the oxidation state of vanadium could lead to a difference in reactivity, which could lead to LSV behaving differently over time compared to its initial behavior. This could have ramifications with modeling and durability predictions. Second, increased sulfur doping eventually leads to lattice expansion (due to the size difference between sulfur and oxygen) and lattice strain within the LSV sub-sample. This strain will eventually become large enough that

oxygen will be removed from the lattice to alleviate this strain. If enough oxygen is expelled due to strain, then the crystal structure or the crystallinity of LSV could change and alter its physical properties, such as electronic/ionic conductivity and sulfur adsorption. Third, strontium segregation, especially at temperatures between 600-700°C can lead to the formation of $SrVO_3$, causing additional oxygen loss from the LSV lattice. The segregation of strontium can lead to crystal structure changes in LSV, similar to the incorporation of strain, but also the addition of $SrVO_3$ (a secondary phase) can have radical implications of the catalytic performance of LSV. If $SrVO_3$ has a significantly lower electronic/ionic conductivity, and becomes a statistically significant phase fraction, then the overall sample conductivity would be reduced. Finally, the selection of the balance gas or solution appears important as it can a greater affinity to LSV, compared to sulfur, and significantly lower sulfur adsorption as was seen with the methanol samples. This is important to understand since potentially blending a small amount of gaseous methanol to methane or hydrogen could inhibit sulfur adsorption further. Further investigation into other fuel types, especially polar molecules, could lead to further improved sulfur tolerance and would a great avenue to explore in future papers.

In conclusion, understanding how sulfur contamination and balance fuels impact LSV over time is crucial to developing and modeling a solid oxide fuel cell anode catalyst that has strong initial performance and does not degrade easily. The use of methanol fuel and potentially other polar alcohol fuels resulted in the lowest sulfur adsorption on LSV and the most accurate initial Rietveld vanadium oxidation state calculations. Despite its increased sulfur tolerance, methanol is a hydrocarbon fuel and may not be used actively used in the future with a hydrogen infrastructure. If hydrogen is the realistic fuel choice available, then additional modeling and elemental doping may be required to change its chemical formulation and improve its sulfur tolerance further. The results and insights presented in this paper will be incredibly useful in those endeavors.

References

[1] F. Faraji, I. Safarik, O. Strausz, E. Yildirim and M. Torres, "The direct conversion of hydrogen sulfide to hydrogen and sulfur," *Int. J. Hydrogen Energy,* vol. 23, no. 6, pp. 451-456, 1998.

[2] N. Hasnan, S. Timmiati, K. Lim, Z. Yaakob, N. Kamaruddin and L. Teh, "Recent developments in methane decomposition over heterogeneous catalysts: an overview," *Mater. Renew. Sustain. Energy,* vol. 9, no. 8, pp. 1-18, 2020.

[3] E. Valimaki, L. Yli-Varo, H. Romar and U. Lassi, "Carbons Formed in Methane Thermal and Thermocatalytic Decompositon Processes: Properties and Applications," *C - Jounral of Carbon Research,* vol. 7, p. 50, 2021.

[4] T. Li, H. Zhang, Y. Li, J. Li, J. Wang and J. Xiao, "Theoretical Study on the Unimolecular Pyrolysis of Thiophene and Modeling," *ACS Omega,* vol. 6, pp. 20471-20482, 2021.

[5] C. Fletcher, "The thermal decomposition of methyl alcohol," *Proc. R. Soc. A,* vol. 147, no. 860, pp. 119-128, 1934.

[6] X. Hou, K. Ohta, Y. Kimura, Y. Tamenori, K. Tsuruta, K. Amezawa and T. Nakamura, "Lattice Oxygen Instability in Oxide-Based Intercalation Cathodes: A Case Study of Layered LiNi1/3Co1/3Mn1/3O2," *Adv. Energy Mater.,* vol. 11, no. 30, p. 2101005, 2021.

[7] F. Meng, Y. Ji, S. Chen and Q. Zhang, "Electrochemistry Induced Giant and Reversible Deformation in Oxides," *Adv. Funct. Mater.,* vol. 30, no. 15, p. 1908826, 2020.

[8] F. Wang, L. Mao, X. Qi, L. Xia, H. Xia and J. Mao, "Sulfur-Induced Abundnace Oxygen Vacanies in Hollow Silica Microspheres Toward Super Anode," *J. Chem. Eng.,* vol. 418, p. 129397, 2021.

[9] L. Zhuang, Y. Jia, H. Liu, Z. Li, M. Li, L. Zhang, X. Wang, D. Yang, Z. Zhu and X. Yao, "Sulfur-Modified Oxygen Vacanies in Iron-Cobalt Oxide Nanosheets: Enabling Extremely High Activity of the Oxygen Evolution Reaction to Achieve the Industrial Water Splitting Bemchmark.," *Angew. Chem., Int. Ed. Engl.,* vol. 59, no. 34, pp. 14664-14670, 2020.

[10] H. Qiu, R. Zhang and Y. Zhang, "Na+ Lattice Doping Induces Oxygen Vacancies to Achieve High Capacity and Mitigate Voltage Decay of Li-Rich Cathodes," *Int. J. Mol. Sci.,* vol. 24, no. 9, p. 8035, 2023.

[11] H. Chen, C. Lim, M. Zhou, Z. He, X. Sun, X. Li, Y. Ye, T. Tan, H. Zhang, C. Yang, J. Han and Y. Chen, "Activating Lattice Oxygen in Perovskite Oxide by B-Site Cation Doping for Modulated Stability and Activity at Elevated Temperatures," *Adv. Sci.,* vol. 8, no. 22, p. 2102713, 2021.

[12] K. Koo, K. Kim, J. Kim, H. Kwon, J. Han and W. Jung, "Sr Segregation in Perovskite Oxides: Why It Happens and How It Exists," *Joule,* vol. 2, no. 8, pp. 1476-1499, 2018.

[13] Z. Feng, Y. Yacoby, M. Gadre, Y.-L. Lee, W. Hong, H. Zhou, M. Biegalski, H. Christen, S. Adler, D. Morgan and Y. Shao-Horn, "Anomalous Interface and Surface Strontium Segregation in (La1-ySry)CoO4±δ/La1-xSrxCoO3-δ Heterostructured Thin Films," *J. Phys. Chem. Lett.,* vol. 5, no. 6, pp. 1027-1034, 2014.

[14] Y. Orikasa, E. Crumlin, S. Sako, K. Amezawa, T. Uruga, M. Biegalski, H. Christen, Y. Uchimoto and Y. Shao-Horn, "Surface Strontium Segregation of Solid Oxide Fuel Cell Cathodes Proved by In Situ Depth-Resolved X-ray Absorption Spectroscopy," *ECS Electrochem. Lett.,* vol. 3, no. 4, p. F23, 2014.

[15] N. Patel, R. Utter, D. D. and M. Pecht, "Surface Degradation of Strontium-based Perovskite Electrodes of Solid Oxide Fuel Cells," *J. Power Sources,* vol. 438, no. 31, p. 227040, 2019.

[16] J. Slater, "Atomic Radii in Crystals," *J. Chem. Phys.,* vol. 41, no. 10, pp. 3199-3204, 1964.

[17] E. Clementi, D. Raimondi and W. Reinhardt, "Atomic Screening Constants from SCF Functions. II. Atoms with 37 to 86 Electrons.," *J. Chem. Phys.,* vol. 47, no. 4, pp. 1300-1307, 1967.

[18] S. A. Materials, "Stanford Advanced Materials," 2023. [Online]. Available: https://www.samaterials.com/vanadium/2077-vanadium-oxide-powder.html. [Accessed 2023].

[19] W. Gu, H. Wang and K. Wang, "Nickel L-edge and K-edge X-ray Absorption Spectroscopy of Non-Innocent Ni[(S2C2(CF3)2]2" Series (n=-2, -1. 0): Direct Probe of Nicel Fractional Oxidation State Changes," *Dalton Trans.,* vol. 43, pp. 6406-6413, 2014.

[20] R. Khan, J. Bashir, N. Iqbal and K. M.N., "Crystal structure of LaVO3 by Rietvel refinement method," *Mater. Lett.,* vol. 58, no. 11, pp. 1737-1740, 2004.

[21] C.-Y. Liu, S.-Y. Tsai, C.-T. Ni and K.-Z. Fung, "Effect of Strontium-Doped Lanthanum Vanadate on Crystal Structure, Conductivity and Vanadium Valence State of a La1-xSrxVO3 Anode in a Reducing Environment," *J. Electron. Mater.,* vol. 46, no. 4, pp. 2301-2308, 2017.

[22] M. Anas, A. Jai, M. Gupta, A. Sagdeo, S. Yusuf, T. Maitra and V. Malik, "Structural and magnetic properties of LaVO3 - Absence of anomalous diamagetism," *Ceram. Int.,* vol. 49, no. 6, pp. 9672-9680, 2023.

[23] Z. Cheng, S. Zha, L. Aguilar and M. Liu, "Chemical, electrical, and thermal properties of strontium doped lanthanum vanadate," *Solid State Ionics,* vol. 176, pp. 1921-1928, 2005.

[24] A. Wold and R. Ward, "Perowskite-Type Oxides of Cobalt, Chromium and Vanadium with Some Rare Earth Elements," *J. Am. Chem. Soc.,* vol. 76, no. 4, pp. 1029-1030, 1954.

[25] M. Brahlek, V. Stoica, J. Lapano, L. Zhang, H. Akamatsu, I.-C. Tung, V. Gopalan, D. Walko, H. Wen, J. Freeland and R. Engel-Herbert, "Structural dynamics of LaVO3 on the nanosecond time scale," *Struct. Dyn.,* vol. 6, no. 1, p. 014502, 2019.

[26] C.-Y. Liu, S.-Y. Tsai, C.-T. Ni and K.-Z. Fung, "Effect of Strontium-Doped Lanthanum Vanadate on Crystal Structure, Conductivity and Vanadium Valence State of a La1-xSrxVO3 Anode in a Reducing Environment," *J. Electron. Mater.,* vol. 46, pp. 2301-2308, 2017.

[27] V. K. E. Komarewsky, "Hydrogenolysis of Thiophene over Vanadium Oxide," *Ind. Eng. Chem.,* vol. 43, no. 6, pp. 1414-1418, 1951.

[28] W. Peng, Z. Aiguo, T. Huiping and L. Hun, "Reaction Mechanism of Thiophene on Vanadium Oxide under FCC Operating Conditions," *Petroleum Processing and Petrochemicals,* vol. 36, no. 7, p. 41, 2005.

[29] F. Elfeninat, C. Fredriksson, E. Sacher and A. Selmani, "A Theoretical Investigation of the Interactions between Thiophene and Vanadium, Chromium, Copper, and Gold," *J. Chem. Phys.,* vol. 102, pp. 6153-6158, 1995.

[30] S. Hanafi, H. El-Syed, M. Elmelawy and E.-S. Sultan, "Study of the Role of Lanthanum Containing Titania in Hydrogenolysis of Thiophene and Gas Oil," *Energ. Source Part A.,* vol. 31, no. 10, pp. 831-842, 2009.

[31] D. Goodacre, M. Blum, C. Buechner, V. Jovic, J. Franklin, S. Kittiwatanakul, T. Sohnel, H. Bluhm and K. Smith, "Methanol Adsorption on Vanadium Oxide Surfaces Observed by Ambient Pressure X-ray Photoelectron Spectroscopy," *J. Phys. Chem. C.,* vol. 125, pp. 23192-23204, 2021.

[32] J. Dobler, M. Pritzsche and J. Sauer, "Oxidation of Methanol to Formaldehyde on Supported Vanadium Oxide Catalysts Compared to Gas Phase Molecules," *J. Am. Chem. Soc.,* vol. 127, pp. 10861-10868, 2005.

[33] G. Deo and I. Wachs, "Reactivity of Supported Vandium Oxide Catalysts: The Partial Oxidation of Methanol," *J. Catal.,* vol. 146, pp. 323-334, 1994.

[34] Y. Romanyshyn, S. Guimond, H. Kuhlenbeck, S. Kaya, R. Blum, H. Niehus, S. Shaikhutdinov, V. Simic-Milosevic, N. Nilis, H.-J. Freund, M. Ganduglia-Pirovano, R. Fortrie, J. Dobler and J. Sauer, "Selectivity in Methanol Oxidation as Studied on Model Systems Involving Vanadium Oxides," *Top. Catal.,* vol. 50, pp. 106-115, 2008.

[35] A. De Asha, J. Critchley, A. Siokou and R. Nix, "Interaction of Methanol with Lanthanum Oxide Surfaces and LaOx/Cu(111) Interfaces," *Phys. Chem. Chem. Phys.,* vol. 2, pp. 4758-4767, 2000.

[36] F. Meng, C. Dai, Z. Liu, S. Luo, J. Ge, Y. Duan, G. Chen, C. Wei, R. Chen, J. Wang, D. Mandler and Z. Xu, "Methanol Electro-Oxidation to Formate on Iron-Substituted Lanthanum Cobaltite Perovskite Oxides," *eScienec,* vol. 2, pp. 87-94, 2022.